Bimetal Doping in Nanoclusters: Synergistic or Counteractive?

Nan Yan,[†,§] Lingwen Liao,[†,§] Jinyun Yuan,[‡,§] Yue-jian Lin,[∥,§] Lin-hong Weng,[*,∥] Jinlong Yang,[*,‡] and Zhikun Wu[*,†]

[†]Key Laboratory of Materials Physics, Anhui Key Laboratory of Nanomaterials and Nanostructures, Institute of Solid State Physics, Chinese Academy of Sciences, Hefei 230031, China

[‡]Hefei National Laboratory for Physics Sciences at the Microscale, University of Science and Technology of China, Hefei, Anhui 230026, China

[∥]Shanghai Key Laboratory of Molecular Catalysis and Innovative Material, Department of Chemistry, Fudan University, Shanghai 200433, China

ⓢ Supporting Information

ABSTRACT: Doped nanoparticles (especially bimetal doped nanoparticles) have attracted extensive interest not only for fundamental scientific research but also for application purposes. However, their indefinite composition (structure) and broad distribution hinder an insightful understanding of the interaction between these invasive metals in bimetal doped nanoparticles. Fortunately, atom-precise bimetal doped ultra-small nanoparticles (nanoclusters) provide opportunities to obtain such insights. However, atom-precise trimetal nano-clusters and their structures have rarely been reported. Here, we successfully dope thiolated Au_{25} nanoclusters with Hg and

Ag successively by using a biantigalvanic reduction method. We then fully characterize the as-obtained trimetal nanoclusters using multiple techniques (including single-crystal X-ray crystallography), and we demonstrate that the mercury and silver dopings exhibit not only a synergistic but also a counteractive influence on some of the physicochemical properties of Au_{25}.
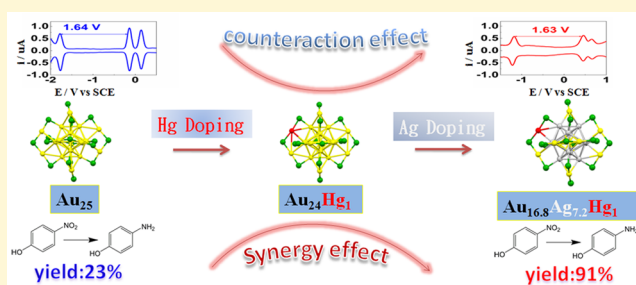
1. INTRODUCTION

The doping of metal nanoparticles by foreign metals is interesting and provides enormous opportunities for engineer-ing metal nanoparticles.[1−6] Doping metal nanoparticles with atom precision is of great importance to subtly tune the properties of metal nanoparticles and gain insight into the tuning mechanism.[7−13] However, it is challenging to achieve atom-precise doping for nanoparticles larger than 3 nm. The recent advances in atom-precise thiolated nanoparticles (so-called nanoclusters) synthesis[14−37] provide possibilities for such doping, and over a dozen atom-precise bimetal nanoclusters such as $Au_{13}Cu_x$,[38] $Au_{12+n}Cu_{32}$,[39] $Au_{24}Pd$,[40,41] $Au_{24}Pt$,[42,43] $Au_{25−x}Ag_x$,[44] $Au_{25−x}Cu_x$,[45,46] $Au_{36}Pd_2$,[47] $Au_{38−x}Ag_x$,[48] $Au_{144−x}Ag_x$,[49] $Au_{(144,145−x)}Cu_x$,[50] $Ag_{24}Pd$,[51] and $Ag_{24}Pt$[51] were synthesized using the synchro method (that is, the bimetal nanoparticles were formed after the mixed metal salts were synchronously reduced). Very recently, even bimetals-doped nanoclusters (trimetal nanoclusters) were obtained.[52−54] However, the dopant position and the interaction between the foreign metals in bimetal doped nanoclusters are unknown, although a synergy effect was once reported for trimetal nanoparticles,[55−58] whose indefinite structure and broad distribution hinder an insightful investigation of the interaction between two foreign metals.

To unravel these fundamental issues, more work must be done. Developing a novel synthesis method is of primary

importance because, on the one hand, it can provide materials for subsequent studies of structures and properties and because, on the other hand, there are few reports on the synthesis of trimetal nanoclusters employing methods other than the synchro method.[53] The recently revealed unexpected anti-galvanic reduction (AGR; it is opposite to the classic galvanic reduction,[59−63] but does not violate thermodynamics) provides a novel strategy for the synthesis of atom-precise alloy nanoparticles,[64] using which we have actually successfully synthesized atomically precise $Au_{25}Ag_2(PET)_{18}$ (PET = SC_2H_4Ph),[65] $Au_{24}Hg_1(PET)_{18}$,[66] and $Au_{24}Cd_1(PET)_{18}$[67] with moderate or high yields. It has also been recently shown that the AGR technique is not only ion-dependent but also ion-precursor and ion-dose dependent.[68] Thus, by tailoring the reaction parameters (e.g., ion species, ion-precursor), one can obtain trimetal nanoclusters, as verified in our experiments. Below, we present the unique synthesis and atomic structure of a novel trimetal nanocluster. Importantly, we present for the first time that the mercury and silver doping exhibit not only a synergistic but also a counteractive influence on some of the physicochemical properties of $Au_{25}(PET)_{18}^{-}$ (Au_{25} for short).

2. EXPERIMENTAL SECTION

2.1. Materials. Tetrachloroauric(III) acid ($HAuCl_4 \cdot 4H_2O$, > 99.9% metals basis), tetraoctylammonium bromide (TOAB, ≥ 98.0%,), 2-phenylethanethiol (PET, 99%, Sigma-Aldrich), Bu_4NPF_6 (99%, Sigma-Aldrich), sodium borohydride ($NaBH_4$, 99.8%, Shanghai Chemical Reagent Co., Ltd.), $Hg(NO_3)_2 \cdot 1/2H_2O$ (99.0%, Shanghai Chemical Reagent Co., Ltd.), and $AgNO_3$ (99.8%, Shanghai Chemical Reagent Co., Ltd.) were used as reagents. Solvents, including THF, ethanol, toluene, acetonitrile, CH_2Cl_2, H_2SO_4, and methanol (MeOH), were purchased from Shanghai Chemical Reagent Co., Ltd. The water used in all experiments was ultrapure (resistivity 18.2 MΩ cm) and produced by a Milli-Q NANO pure water system. All chemicals were used as received.

2.2. Synthesis of $Au_{24}Hg_1(PET)_{18}$. The nanoclusters were synthesized by reacting anion $Au_{25}(PET)_{18}$ (the synthesis of which was described in a previous publication[69]) with $Hg(NO_3)_2$.[66] First, 24 mg of $Au_{25}(PET)_{18}$ clusters was dissolved in 8 mL of acetonitrile; then an aqueous solution of $Hg(NO_3)_2$ (1 equiv per mole of $Au_{25}(SR)_{18}$) was rapidly added under vigorous and continuous stirring. After 1.5 h, 10 μL of PET dissolved in 300 μL of acetonitrile was added to the solution. The product that precipitated out of the solution was collected, thoroughly washed with MeOH, and then recrystallized in a solvent mixture of 1 mL of toluene and 4 mL of acetonitrile.

2.3. Synthesis of $Au_{24-x}Ag_xHg_1(PET)_{18}$, $Au_{25-x}Ag_x$ $(PET)_{18}$, and PET-Protected Hg Nanoparticles. To synthesize the $Au_{24-x}Ag_xHg_1(PET)_{18}$ nanoclusters, 1 mL of ethanol solution of $AgNO_3$ (0.00675 mmol) was first mixed with 0.05 mL of PET under vigorous stirring. After 30 min of stirring, the contents were put in the centrifuge. The precipitate was then washed with ethanol at least 3 times to remove the excess thiol and was then dried under vacuum to yield white powder Ag(I)-PET complex. The synthesis of Hg(II)-PET complex was similar to the synthesis of Ag(I)-PET complex except that the $AgNO_3$ was replaced with $Hg(NO_3)_2$. Next, 5 mg of $Au_{24}Hg_1(PET)_{18}$ nanoclusters was dissolved in 3 mL of toluene. The as-obtained Ag(I)-PET complex was then added to the solution of $Au_{24}Hg_1(PET)_{18}$. After stirring for 24 h at room temperature, the reaction mixture was centrifuged to remove the unreacted Ag(I)-PET complex, and the reaction was stopped by adding a large amount of MeOH. Next, the precipitates were collected and thoroughly washed with MeOH. Single-crystal growth was then performed via the vapor diffusion of pentane into a CH_2Cl_2 solution of the as-obtained product.

The synthesis of $Au_{25-x}Ag_x(PET)_{18}$ was similar to that of $Au_{24-x}Ag_xHg_1(PET)_{18}$, except that the $Au_{24}Hg_1(PET)_{18}$ was replaced with $Au_{25}(PET)_{18}$.

The synthesis of PET-protected Hg nanoparticles was similar to that of $Au_{25}(PET)_{18}$ except that the solvent of tetrahydrofuran was replaced with methanol.

2.4. Characterization. All UV−vis/NIR absorption spectra were acquired in the range of 190−900 nm using a UV2600 spectrophotometer. The diffraction data of the single crystals were collected on an Agilent Gemini S Ultra diffractometer using Cu Kα radiation, and the crystal structure was determined by direct methods and refined using the full-matrix least-squares methods in the SHELXL-2013 program (Sheldrick, 2013). Matrix-assisted laser desorption ionization mass spectrometry (MALDI-MS) was performed on an autoflex

Speed TOF/TOF mass spectrometer (Bruker) in positive mode, and the Compass Isotope Pattern was used to simulate the isotopic pattern. Trans-2-[3-(4-*tert*-butylphenyl)-2-methyl-2-pro-penylidene] malononitrile (DCTB) was used as the matrix, and the molar ratio of cluster to matrix was 1:600. Electrospray ionization mass spectra (ESI-MS) were recorded on a Waters Q-TOF mass spectrometer using a Z-spray source. The sample was first dissolved in toluene (∼0.5 g/L) and then diluted (2/1 v/v) with ethanol solution which contains 50 mmol CsOAc. The sample was directly infused into the chamber at 5 μL/min. The source temperature was kept at 70 °C, the spray voltage was 2.20 kV, and the cone voltage was adjusted at 60 V. X-ray photoelectron spectroscopy (XPS) measurements were conducted on an ESCALAB 250Xi XPS spectrometer (Thermo Scientific, America), using a mono-chromatized Al Kα source and equipped with an Ar^+ ion sputtering gun. All binding energies were calibrated using the C (1s) carbon peak (284.8 eV). Thermal gravimetric analysis (TGA) (∼3 mg sample used) was conducted in a N_2 atmosphere (flow rate ∼50 mL/min) on a TG/DTA 6300 analyzer (Seiko Instruments, Inc.), and the heating rate was 10 °C/min. NMR spectra were recorded on a Bruker AC-400 FT spectrometer (400 MHz) using tetramethylsilane as an internal reference.

2.5. Electrochemistry. We used a conventional three-electrode system for the experiments. Carbon rods and a Saturated Calomel Electrode (SCE; with saturated KCl solution) were employed as a counter electrode (CE) and reference electrode (RE), respectively. The working electrode (WE) was a Pt disk electrode (1 mm diameter). Before use, the WE was polished first on emery paper of decreasing grades and then via Al_2O_3 powders down to 50 nm in size; it was then cleaned electrochemically by potential-cycling in 0.5 M H_2SO_4 solution. The electrode was then rinsed thoroughly with ultrapure water (18.2 M). The potentials of the electrode were controlled by a potentiostat (Zahner, Germany).

3. RESULTS AND DISCUSSION

Au_{25} was chosen as the matrix nanocluster because it is the most studied type of nanocluster.[65−67] In a typical doping, briefly (for details, see the Experimental Section), Au_{25} was first reacted with Hg^{2+} ions to prepare $Au_{24}Hg_1(PET)_{18}$ ($Au_{24}Hg_1$ for short), as shown in our previous work.[66] Then, $Au_{24}Hg_1$ was mixed with Ag(I)-PET complex under vigorous stirring at room temperature. After stirring for 24 h, the reaction was centrifuged to remove the unreacted Ag(I)-PET complex and terminated by adding a large amount of CH_3OH. Next, the precipitates were collected and washed with CH_3OH three times. Single-crystal growth was then performed via the vapor diffusion of pentane into a CH_2Cl_2 solution of the as-obtained nanoclusters. Dark single crystals were formed after 1−2 days with a yield of 90% (based on the gold atoms in $Au_{24}Hg_1$). $Au_{24}Hg_1$ nanoclusters can decompose when silver salt is employed as the ion-precursor instead of the Ag-PET complex due to its strong tendency to oxidize (Figure S1).[68,70,71] Because AGR was employed twice during the bimetal doping process, the introduced synthesis method can be dubbed "bi-antigalvanic reduction" (BAGR). For comparison (see below), $Au_{25-x}Ag_x(PET)_{18}$ ($Au_{25-x}Ag_x$ for short) was prepared by reacting Au_{25} with Ag(I)PET complex under similar conditions.[68]

The UV−vis/NIR absorption spectrum of the as-obtained crystals dissolved in CH_2Cl_2 is shown in Figure 1a. The spectra
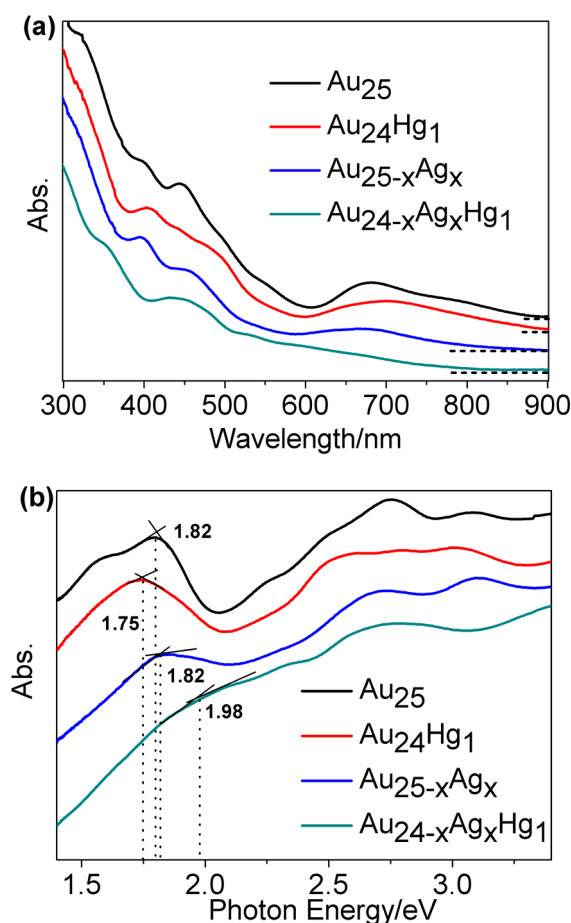
Figure 1. (a) UV−vis/NIR absorption and (b) photon energy scale spectra of Au_{25}, $Au_{24}Hg_1$, $Au_{25-x}Ag_x$ and $Au_{24-x}Ag_xHg_1$, dissolved in CH_2Cl_2.

of Au_{25}, $Au_{24}Hg_1$, $Au_{25-x}Ag_x$ are also presented in Figure 1a for comparison. It can be seen that the as-obtained crystals exhibit a spectrum that is distinctly different from those of the other three nanoclusters, with two prominent peaks centered at 350 and 450 nm and an indistinctive shoulder peak at 530 nm. Photon energy scale spectra are also shown in Figure 1b for comparison: the monogold Au_{25} nanoclusters exhibit a prominent peak at ~1.81 eV that corresponds to the core sp → sp intraband transition,[72] and $Au_{24}Hg_1$ and $Au_{25-x}Ag_x$ exhibit broad peaks at ~1.75 and ~1.82 eV, respectively. Nevertheless, the as-obtained crystals have a weak broad peak at ~1.98 eV. MALDI-TOF-MS is employed to identify their compositions. As shown in Figure S2, the mass spectrum of Au_{25} displays two peaks at m/z 7394 and 6056, which are assigned to $[Au_{25}(PET)_{18}]^-$ and $[Au_{21}(PET)_{14}]^-$ (acquired in negative ionization mode), respectively. $Au_{25-x}Ag_x$ exhibits the same fragmentation mode with Au_{25} (Figure S3). The series of peaks with equidistant intervals (~89 m/z) between 7000 and 7500 m/z indicate that an indeterminate number of gold atoms in the Au_{25} are replaced by silver atoms. Due to the ready removal of the outer-shell Hg atom, $Au_{24}Hg_1$ shows two fragment peaks at m/z 7062 and 5756 in the mass spectrum as reported previously,[66] which are assigned to $[Au_{24}(PET)_{17}]^+$ and $[Au_{20}(PET)_{13}S_1]^+$ (Figure S4), respectively. The as-obtained novel product also exhibits a similar fragmentation mode to that of $Au_{24}Hg_1$ (Figure S5), which suggests that the Hg is included in the newly formed nanoclusters in a similar

fashion to its inclusion in $Au_{24}Hg_1$ and is not replaced by Ag during the second AGR process. The equidistant peaks between m/z 6400 and 6700 indicate that silver atoms are also included in the newly formed nanoclusters. Taken together, the above experimental results indicate that the as-obtained novel product contains Au, Hg and Ag elements.

Electrospray ionization mass spectrometry identifies a series of peaks with the M/Z values corresponding to $[Au_{19-x}Ag_{5+x}Hg_1(PET)_{18}+2Cs]^{2+}$ ($x = 0-3$), among which the most extensive peak centered at ~3521 M/Z is assigned to $[Au_{17}Ag_7(PET)_{18}+2Cs]^{2+}$. The assignments are further confirmed by the excellent agreements between the experimental and simulated isotopic patterns (see Figure S6). The composition and structure of the novel product are further analyzed by single crystal X-ray diffraction, as shown in Figure 2, which indicates that it still has the core−shell framework of
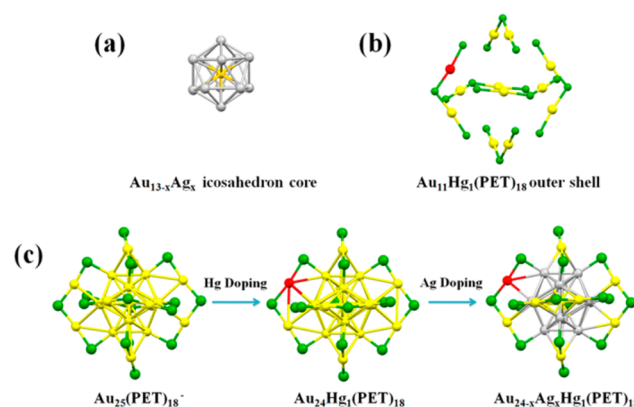

Figure 2. X-ray crystal structure of $Au_{24-x}Ag_xHg_1$: (a) $Au_{13-x}Ag_x$ icosahedron (core andinner-shell), (b) outer-shell and (c) formation process. Au, yellow; Hg, red; Ag, white; S, green; C and H atoms are omitted for clarity.

Au_{25}, with ~7.2 icosahedron gold atoms replaced by silver atoms (Figure 2a). X-ray crystallography can differentiate Ag from Au but cannot differentiate between Hg and Au due to the crystallographic similarity of Hg and Au atoms. However, the similar fragmentation modes in the mass spectra for $Au_{24}Hg_1$ and the novel product indicate that the Hg atom occupies the outer-shell of the as-prepared trimetal nanocluster (Figure 2b), similar to the case of $Au_{24}Hg_1$.[66] Single-point energy calculations exclude the possibility of the core occupation by Hg because its energy is higher than that of the other two by ~1.7 eV. Further, time-dependent density functional theory (TDDFT, with the pure functional PBE) calculations indicate that the probability of Hg occupying the outer-shell is greater than that of it occupying the inner-shell or core, because the outer-shell simulation best matches the experimental spectrum with the feature peaks centered at 350, 450, and 530 nm (see Figure 3). Notably, this method has been proven to give results in good agreement with experimental data obtained for ligand-protected Au nanoclusters.[73] For example, it has been used to simulate the spectra of $Au_{18}(SR)_{14}$,[74] $[Au_{20}(PPhy_2)_{10}Cl_4]Cl_2$,[75] $Au_{38}(SR)_{24}$,[76] $Au_{40}(SR)_{24}$,[77] $Au_{55}(PPh_3)_{12}Cl$,[78] and $Au_{24}Cd$-$(PET)_{18}$.[67] We also used this method to reproduce the spectra of well-established clusters, such as $Au_{25}(PET)_{18}$ and $HgAu_{24}(PET)_{18}$ (see Figure S7 and S8). For the Hg occupying the outer-shell, more evidence will be provided (vide infra). Thus, the total structure evolution of the as-prepared trimetal nanoclusters is shown in Figure 2c: first, the Hg heteroatom
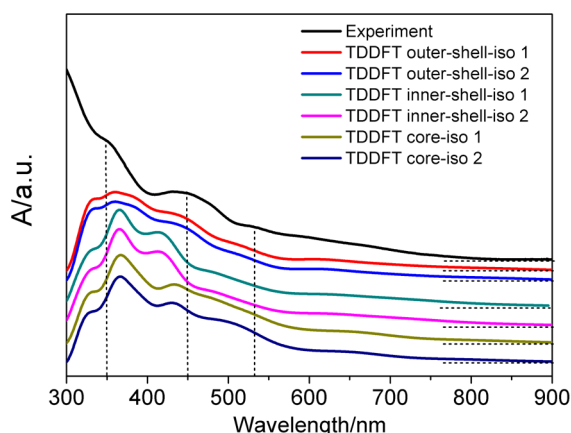
Figure 3. Comparison of the experimental and time-dependent density functional (TDDFT) calculated UV−vis/NIR absorption spectra of $Au_{24-x}Ag_xHg_1$ with various Hg occupying sites (outer-shell, inner-shell, and core). For the calculated cases, only the lowest (iso 1) and the second-lowest (iso 2) energy isomers for Hg occupying the core, inner-shell, or outer-shell of $Au_{17}Ag_7Hg_1$ are presented for clarification. Note: the suffixes iso 1 and iso 2 represent the two stablest isomers in every case including the core, inner-shell or outer-shell occupying of mercury, and for their detailed structures, see Figure S9.

dopes in the outer-shell of $Au/Au_{12}/Au_{12}$ structured Au_{25},[66] and the Ag heteroatoms then selectively incorporate in the 12 vertices of the Au_{13} icosahedra in the second AGR process.[79−81] It is interesting that one Hg vs 7.2 silver atoms is incorporated in the $Au_{24-x}Ag_xHg_1(PET)_{18}$ ($Au_{24-x}Ag_xHg_1$ for short) nanocluster. The superatom[82] (superanion[83]) concept could provide an explanation for this result. One gold replacement by Hg in Au_{25} nanocluster could result in an 8-electron shell closing electronic structure while additional Hg replacements destabilize the shell closing structure; thus, additional Hg replacements are not favorable. However, Ag has similar valent electron configuration as gold; thus, the multiple silver substitution is permitted within limits because it would not alter the original shell closing structure of $Au_{24}Hg_1$.

X-ray photoelectron spectroscopy (XPS) was employed to confirm the composition revealed by X-ray crystallography. First, the qualitative measurement indicates the existence of all the three metals: Au, Hg, and Ag (see Figure S10). Second, quantitative calculation reveals that the Au/Ag/Hg/S atomic ratio matches well with the one obtained by single crystal X-ray diffraction (see Table S1 for details). Third, the absence of nitrogen element detection implies that the nanocluster might be of electric neutrality without TOA^+ (tetra-*n*-octylammonium) or NO_3^- as a counterion, which is in agreement with the absent observation of counterions in single crystal X-ray crystallography. The Hg $4f_{7/2}$ and Hg $4f_{5/2}$ binding energies of the trimetal nanocluster are 100.35 and 104.57 eV (Figure S11), respectively, which are identical with those of $Au_{24}Hg_1$, implying the Hg outer-shell occupying in $Au_{24-x}Ag_xHg_1(PET)_{18}$ as that in $Au_{24}Hg$.[66] For comparison, the Hg(II)-PET complexes and PET-protected Hg nanoparticles were also prepared and characterized by XPS (see Figures S12 and S13). The Hg 4f binding energies of Hg(II)-PET complexes are much higher than those of the trimetal nanocluster, verifying the occurrence of AGR during the mercury-doping. The Hg 4f binding energies of Hg nanoparticles can be deconvolved into two series: one series of Hg

4f binding energies (Hg $4f_{7/2}$: 99.55 eV; Hg $4f_{5/2}$: 103.63 eV), similar to those of metal Hg (Hg $4f_{7/2}$: 99.5 eV; Hg $4f_{5/2}$: 103.6 eV), can be assigned to the kernel Hg in Hg nanoparticles, and thus, the other series of Hg 4f binding energies (Hg $4f_{7/2}$: 100.33 eV; Hg $4f_{5/2}$: 104.38 eV) can be attributed to the surface Hg which bonds to thiolates. Interestingly, the Hg 4f binding energies of the surface Hg in Hg nanoparticles are almost identical to the Hg 4f binding energies in the $Au_{24-x}Ag_xHg_1(PET)_{18}$ nanocluters, further indicating the Hg outer-shell occupying in the trimetal nanoclusters. The fact that the Ag 3d binding energies of the inner-shell occupied silver in $Au_{24-x}Ag_xHg_1(PET)_{18}$ (see Figure S14) are close to those of metal silver[64] provides evidence for the above deduction. TGA (Figure S15) reveals a weight loss of 34.5%, which is very close to the expected value (34.8%) for nanoclusters with a composition of $Au_{16.8}Ag_{7.2}Hg_1(PET)_{18}$ ($Au_{16.8}Ag_{7.2}Hg_1$ for short). Of note, a weight loss of 2.7% from 230 to 500 °C is caused by the loss of mercury atoms, similar to the case of $Au_{24}Hg_1$,[66] thus providing additional support for the outer-shell occupation of Hg in the trimetal nanocluster. NMR also provides evidence for the position of Hg (Figure S16). Although broadness and overlap of the peaks are found in the ^1H NMR spectrum of $Au_{24-x}Ag_xHg_1$ due to the enclosing of multiple heteroatoms, it is still obvious that the ^1H NMR spectrum profile of $Au_{24-x}Ag_xHg_1$ shows closer similarities to that of $Au_{24}Hg_1$ than those of $Au_{25-x}Ag_x$ (see Figure S16) and $Au_{24}Pd(Pt)_1$,[42] which indicates the Hg positions in both $Au_{24-x}Ag_xHg_1$ and $Au_{24}Hg_1$ are similar. Thus, deduced from the NMR results the Hg most probably occupies the outer-shell of $Au_{24-x}Ag_xHg_1$ as the Hg in $Au_{24}Hg_1$ does.

Previous studies have shown that replacing a number of gold atoms in Au_{25} with Ag or Cu results in a modification of the electronic structure.[44−46] Nonetheless, there is no report on how these two types of heteroatoms jointly affect the electronic structure of Au_{25}. Thus, differential pulse voltammetry (DPV), a well-recognized technique,[84] is employed to probe the first oxidation/reduction potential change of Au_{25} after being doped with both Hg and Ag. A comparison of the first oxidation/reduction potential among Au_{25}, $Au_{24}Hg_1$, $Au_{25-x}Ag_x$, and $Au_{24-x}Ag_xHg_1$ is shown in Figures 4 and 5. The Hg-doping decreases the electrochemical gap of Au_{25} by 0.12 V. In strong contrast, the Ag-doping increases the electrochemical gap of Au_{25} by 0.14 V. Interestingly, the increase in the electrochemical gap from Ag-doping and the decrease from Hg-doping are counterbalanced in the trimetal nanoclusters, which exhibit a similar electrochemical gap to Au_{25} (1.64 vs 1.63 V, see Figure 5). Of note, the ∼ −1.05 V peak is probably due to the Hg dopant, which is supported by the DPV of Hg(II)-PET complexes (Figure S17) This counteractive effect, rather than a synergistic effect, in trimetal nanoclusters has not been previously reported in the literature to the best of our knowledge. It is also not evidence of this counteractive effect because we also find a similar phenomenon in the Raman measurements, as shown in Figure 6. An increase in the Raman signals for benzene ring breathing[85] in phenylethanethiolate of the Au_{25} doped with Ag is counteracted by a Hg-doping induced decrease. It should be noted that the Raman signals are indistinguishable for our measurement conditions without the assistance of plasma silver nanoparticles (Figure S18; for experimental details, see the Supporting Information). Because silver is better at triggering Raman signals than gold, the observed enhancement (∼2×) of Raman signals for the benzene ring breathing mode in the Ag-doped Au_{25} nano-
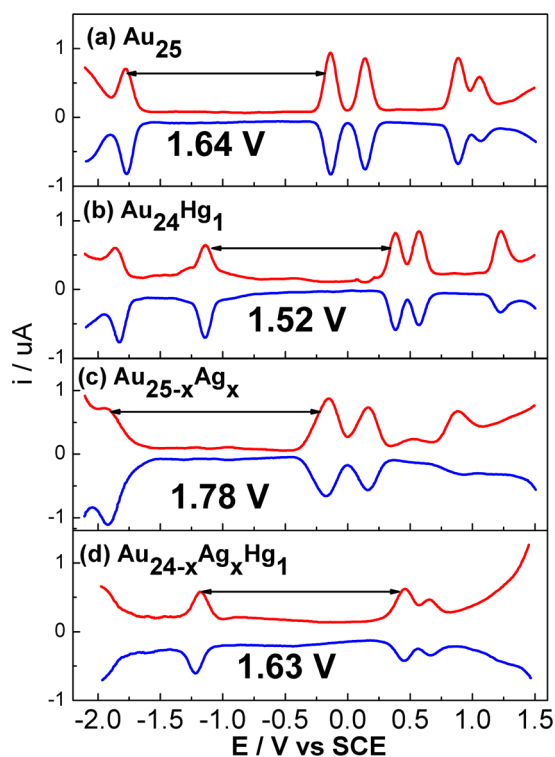
Figure 4. DPV of (a) Au_{25}, (b) $Au_{24}Hg_1$, (c) $Au_{25-x}Ag_x$, and (d) $Au_{24-x}Ag_xHg_1$ at 0.01 V/s in degassed CH_2Cl_2 containing 0.1 M Bu_4NPF_6 with 1 mm diameter Pt working, SCE reference and a carbon rod counter electrode.
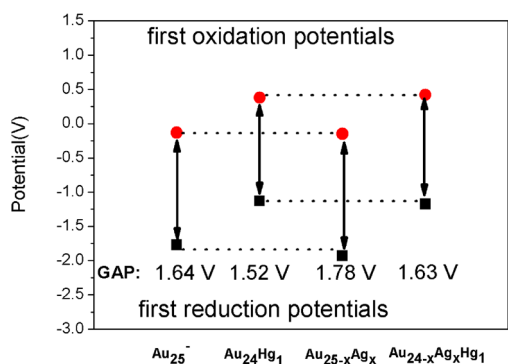

Figure 5. Comparison of first oxidation/reduction potentials of Au_{25}, $Au_{24}Hg_1$, $Au_{25-x}Ag_x$, and $Au_{24-x}Ag_xHg_1$, respectively.

clusters is likely ascribed to the enhanced charge transfer from the metal core to the ligands after Ag-doping, as indicated by theoretical calculations.[86,87]

In contrast, the synergistic effect observed in the bimetal doped nanoclusters is similar to some findings in trimetal nanoparticles.[55−58] For instance, $Au_{24-x}Ag_xHg_1$ exhibits remarkably higher catalytic activity to reduction of 4-nitrobenzene than does the Hg (or Ag)-doped Au_{25} nanoclusters and can be readily recovered by column chromatography for reuse after a minimum of five cycles without obvious loss of catalytic activity (Table 1) (the slight decrease in the yield of 4-aminobenzene is due to the mass loss of catalyst in recycling[70]). The similar UV−vis/NIR (Figure S19) and MALDI-TOF-MS (Figure S20) spectra of $Au_{24-x}Ag_xHg_1$ before and after catalysis indicate that the catalyst is not decomposed during the catalytic process.

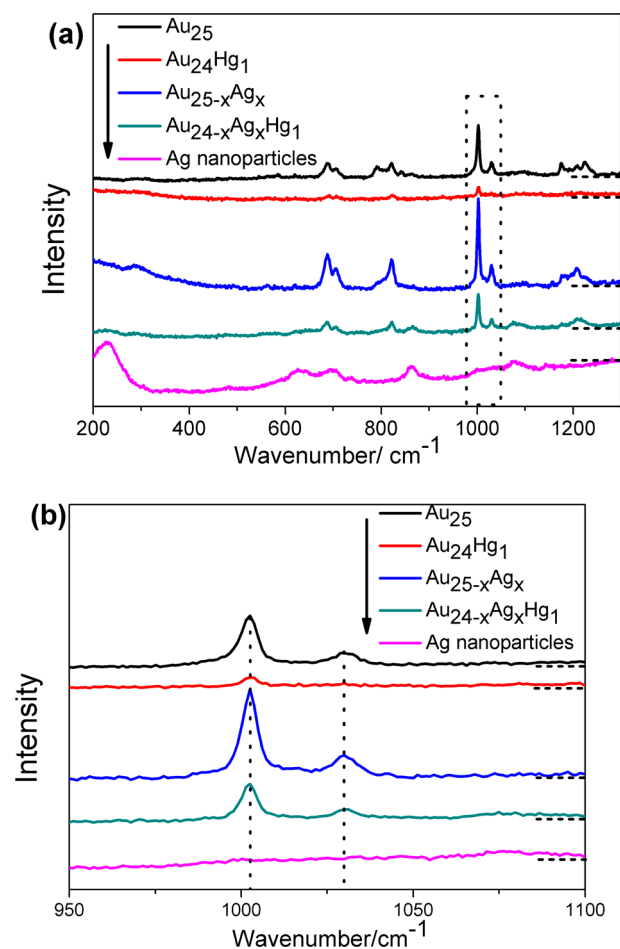**Figure 6.** (a) Full and (b) enlarged Raman spectra of Au_{25}, $Au_{24}Hg_1$, $Au_{25-x}Ag_x$, $Au_{24-x}Ag_xHg_1$, and Ag nanoparticles (substrate), respectively.

Table 1. Comparison of Catalytic Activities of Au_{25}, $Au_{24}Hg_1$, $Au_{25-x}Ag_x$, and $Au_{24-x}Ag_xHg_1$, Respectively

catalyst (0.1 mol %)	yield (%)
$Au_{24-x}Ag_xHg_1$	
1st	91
2nd	87
3rd	85
4th	84
5th	82
Au_{25}	23
$Au_{24}Hg_1$	48
$Au_{25-x}Ag_x$	41

Another illustration of the synergistic effect of bimetal doping is that the codoping of mercury and silver greatly increases the stability of Au_{25} nanoclusters (see Figure S21). Thus, both a counteractive and a synergistic effect were observed in the mercury- and silver-doped Au_{25}, which indicate that the bimetal doping may synergistically strengthen some properties of the matrix nanoclusters but may have nothing to do with (or may even have a negative influence on) other properties. These interesting observations may be extended to other doping

systems and can be understood as follows: the likelihood of synergy or counteraction in metal doping might depend on the matching (consistence) or mismatching (inconsistence) of these different metal atoms in some of their properties or in their spatial arrangement; that is, when these metal atoms match (are consistent) each other in some of their properties or in their spatial arrangement, they might work together, and synergy is thus exhibited (as in the saying "Many hands make light work."). Alternatively, when the metal atoms are mismatched (inconsistent) with each other, they might clash, and the counteractive effect is shown (as in the saying "Too many cooks spoil the broth.").

4. CONCLUSION

In summary, the "bi-antigalvanic reduction" (BAGR) method was introduced to synthesize novel atom-precise trimetallic nanoclusters with high yield (90%). The nanoclusters were determined to be-$Au_{16.8}Ag_{7.2}Hg_1(PET)_{18}$ using multiple techniques such as X-ray crystallography, XPS, and TGA. The atomic structure of $Au_{16.8}Ag_{7.2}Hg_1$ was determined mainly by X-ray crystallography and theoretical calculation, which indicated that mercury and silver dope in the outer-shell and inner-shell of Au_{25}, respectively. This study is also the first to describe the single-crystal structure of thiolated trimetal nanoclusters. More importantly, counteractive effects were found for the first time in the mercury- and silver-doped Au_{25} nanoclusters and coexisted with synergistic effects, which provides important and novel insights into bimetal doping. These novel methods and findings could have important implications for the tuning of metal nanocluster (nanoparticle) compositions, structures, and properties and are expected to trigger more research on the bimetal or even multimetal doping of nanoclusters (nanoparticles).

ASSOCIATED CONTENT

Ⓢ Supporting Information

The Supporting Information is available free of charge on the ACS Publications website at DOI: 10.1021/acs.chemmater.6b03132.

Raman and catalytic test; theoretical method details; UV−vis/NIR absorption, TGA, MALDI-TOF-MS, XPS, and Raman spectra of the mentioned nanocluster(s) (PDF)
Crystal data(CIF)

AUTHOR INFORMATION

Corresponding Authors
*E-mail: zkwu@issp.ac.cn.
*E-mail: jlyang@ustc.edu.cn.
*E-mail: lhweng@fudan.edu.cn.
Author Contributions
§These authors contributed equally (N.Y., L.L., J.Y., and Y.L.).
Notes
The authors declare no competing financial interest.

ACKNOWLEDGMENTS

REFERENCES

(1) Wang, D. S.; Li, Y. D. Bimetallic nanocrystals: liquid-phase synthesis and catalytic applications. *Adv. Mater.* **2011**, *23*, 1044−1060.

(2) Adams, B. D.; Wu, G.; Nigro, S.; Chen, A. Facile Synthesis of Pd− Cd Nanostructures with High Capacity for Hydrogen Storage. *J. Am. Chem. Soc.* **2009**, *131*, 6930−6931.

(3) Xu, D.; Liu, Z. P.; Yang, H. Z.; Liu, Q. S.; Zhang, J.; Fang, J. Y.; Zou, S. Z.; Sun, K. Solution-Based Evolution and Enhanced Methanol Oxidation Activity of Monodisperse Platinum−Copper Nanocubes. *Angew. Chem., Int. Ed.* **2009**, *48*, 4217−4221.

(4) Habas, S. E.; Lee, H.; Radmilovic, V.; Somorjai, G. A.; Yang, P. Shaping binary metal nanocrystals through epitaxial seeded growth. *Nat. Mater.* **2007**, *6*, 692−697.

(5) Sun, S. H.; Murray, C. B.; Weller, D.; Folks, L.; Moser, A. Monodisperse FePt Nanoparticles and Ferromagnetic FePt Nanocrystal Superlattices. *Science* **2000**, *287*, 1989−1992.

(6) Yan, J. M.; Zhang, X. B.; Akita, T.; Haruta, M.; Xu, Q. One-step seeding growth of magnetically recyclable Au@Co core− shell nanoparticles: highly efficient catalyst for hydrolytic dehydrogenation of ammonia borane. *J. Am. Chem. Soc.* **2010**, *132*, 5326−5327.

(7) Yoo, Y.; Seo, K.; Han, S.; Varadwaj, K. S. K.; Kim, H. Y.; Ryu, J. H.; Lee, H. M.; Ahn, J. P.; Ihee, H.; Kim, B. Steering epitaxial alignment of Au, Pd, and AuPd nanowire arrays by atom flux change. *Nano Lett.* **2010**, *10*, 432−438.

(8) Lai, F. J.; Su, W. N.; Sarma, L. S.; Liu, D. G.; Hsieh, C. A.; Lee, J. F.; Hwang, B. J. Chemical dealloying mechanism of bimetallic Pt−Co nanoparticles and enhancement of catalytic activity toward oxygen reduction. *Chem. - Eur. J.* **2010**, *16*, 4602−4611.

(9) Lee, Y. W.; Kim, N. H.; Lee, K. Y.; Kwon, K.; Kim, M.; Han, S. W. Synthesis and characterization of flower-shaped porous Au-Pd alloy nanoparticles. *J. Phys. Chem. C* **2008**, *112*, 6717−6722.

(10) Zhang, J.; Yang, H. Z.; Fang, J. Y.; Zou, S. Z. Synthesis and oxygen reduction activity of shape-controlled Pt3Ni nanopolyhedra. *Nano Lett.* **2010**, *10*, 638−644.

(11) Liu, Z.; Hu, J. E.; Wang, Q.; Gaskell, K.; Frenkel, A. I.; Jackson, G. S.; Eichhorn, B. PtMo Alloy and MoOx@Pt Core− Shell Nanoparticles as Highly CO-Tolerant Electrocatalysts. *J. Am. Chem. Soc.* **2009**, *131*, 6924−6925.

(12) Wetz, F.; Soulantica, K.; Falqui, A.; Respaud, M.; Snoeck, E.; Chaudret, B. Hybrid Co−Au nanorods: controlling Au nucleation and location. *Angew. Chem., Int. Ed.* **2007**, *46*, 7079−7081.

(13) Chen, J.; McLellan, J. M.; Siekkinen, A.; Xiong, Y.; Li, Z. Y.; Xia, Y. Facile synthesis of gold-silver nanocages with controllable pores on the surface. *J. Am. Chem. Soc.* **2006**, *128*, 14776−14777.

(14) Templeton, A. C.; Wuelfing, W. P.; Murray, R. W. Monolayer-protected cluster molecules. *Acc. Chem. Res.* **2000**, *33*, 27−36.

(15) Jadzinsky, P. D.; Calero, G.; Ackerson, C. J.; Bushnell, D. A.; Kornberg, R. D. Structure of a thiol monolayer-protected gold nanoparticle at 1.1 Å resolution. *Science* **2007**, *318*, 430−433.

(16) Jin, R. Quantum sized, thiolate-protected gold nanoclusters. *Nanoscale* **2010**, *2*, 343−362.

(17) Zhang, L. B.; Wang, E. K. Metal nanoclusters: new fluorescent probes for sensors and bioimaging. *Nano Today* **2014**, *9*, 132−157.

(18) Shichibu, Y.; Negishi, Y.; Tsukuda, T.; Teranishi, T. Large-scale synthesis of thiolated Au_{25} clusters via ligand exchange reactions of phosphine-stabilized Au11 clusters. *J. Am. Chem. Soc.* **2005**, *127*, 13464−13465.

(19) Price, R. C.; Whetten, R. L. All-aromatic, nanometer-scale, gold-cluster thiolate complexes. *J. Am. Chem. Soc.* **2005**, *127*, 13750−13751.

(20) Zhu, M.; Lanni, E.; Garg, N.; Bier, M. E.; Jin, R. Kinetically Controlled, High-Yield Synthesis of Au_{25} Clusters. *J. Am. Chem. Soc.* **2008**, *130*, 1138−1139.

(21) Qian, H.; Zhu, Y.; Jin, R. Size-focusing synthesis, optical and electrochemical properties of monodisperse $Au_{38}(SC_2H_4Ph)_{24}$ nanoclusters. *ACS Nano* **2009**, *3*, 3795−3803.

(22) Yuan, X.; Zhang, B.; Luo, Z.; Yao, Q.; Leong, D. T.; Yan, N.; Xie, J. Balancing the Rate of Cluster Growth and Etching for Gram-Scale Synthesis of Thiolate-Protected Au_{25} Nanoclusters with Atomic Precision. *Angew. Chem., Int. Ed.* **2014**, *53*, 4623−4627.

(23) Wu, Z.; MacDonald, M. A.; Chen, J.; Zhang, P.; Jin, R. Kinetic control and thermodynamic selection in the synthesis of atomically precise gold nanoclusters. *J. Am. Chem. Soc.* **2011**, *133*, 9670−9673.

(24) Chen, J.; Zhang, Q. F.; Bonaccorso, T. A.; Williard, P. G.; Wang, L.-S. Controlling gold nanoclusters by diphospine ligands. *J. Am. Chem. Soc.* **2014**, *136*, 92−95.

(25) Crasto, D.; Malola, S.; Brosofsky, G.; Dass, A.; Häkkinen, H. Single crystal XRD structure and theoretical analysis of the chiral $Au_{30}S(St\text{-}Bu)_{18}$ cluster. *J. Am. Chem. Soc.* **2014**, *136*, 5000−5005.

(26) Wang, D.; Padelford, J. W.; Ahuja, T.; Wang, G. Transitions in Discrete Absorption Bands of Au_{130} Clusters upon Stepwise Charging by Spectroelectrochemistry. *ACS Nano* **2015**, *9*, 8344−8351.

(27) Qian, H.; Jin, R. Controlling nanoparticles with atomic precision: the case of $Au_{144}(SCH_2CH_2Ph)_{60}$. *Nano Lett.* **2009**, *9*, 4083−4087.

(28) Levi-Kalisman, Y.; Jadzinsky, P. D.; Kalisman, N.; Tsunoyama, H.; Tsukuda, T.; Bushnell, D. A.; Kornberg, R. D. Synthesis and Characterization of $Au_{102}(p\text{-}MBA)_{44}$ Nanoparticles. *J. Am. Chem. Soc.* **2011**, *133*, 2976−2982.

(29) Mustalahti, S.; Myllyperkiö, P.; Malola, S.; Lahtinen, T.; Salorinne, K.; Koivisto, J.; Häkkinen, H.; Pettersson, M. Molecule-like Photodynamics of $Au_{102}(p\ MBA)_{44}$ Nanocluster. *ACS Nano* **2015**, *9*, 2328−2335.

(30) Wu, Z.; Lanni, E.; Chen, W.; Bier, M. E.; Ly, D.; Jin, R. High yield, large scale synthesis of thiolate-protected Ag_7 clusters. *J. Am. Chem. Soc.* **2009**, *131*, 16672−16674.

(31) Desireddy, A.; Conn, B. E.; Guo, J. S.; Yoon, B.; Barnett, R. N.; Monahan, B. M.; Kirschbaum, K.; Griffith, W. P.; Whetten, R. L.; Landman, U.; Bigioni, T. P. Ultrastable silver nanoparticles. *Nature* **2013**, *501*, 399−402.

(32) Yang, H.; Wang, Y.; Huang, H.; Gell, L.; Lehtovaara, L.; Malola, S.; Hakkinen, H.; Zheng, N. All-thiol-stabilized Ag_{44} and $Au_{12}Ag_{32}$ nanoparticles with single-crystal structures. *Nat. Commun.* **2013**, *4*, 2422.

(33) Rao, T. U. B.; Nataraju, B.; Pradeep, T. Ag_9 quantum cluster through a solid-state route. *J. Am. Chem. Soc.* **2010**, *132*, 16304−16307.

(34) Chakraborty, I.; Govindarajan, A.; Erusappan, J.; Ghosh, A.; Pradeep, T.; Yoon, B.; Whetten, R. L.; Landman, U. The superstable 25 kDa monolayer protected silver nanoparticle: Measurements and interpretation as an icosahedral $Ag_{152}(SCH_2CH_2Ph)_{60}$ cluster. *Nano Lett.* **2012**, *12*, 5861−5866.

(35) Li, G.; Lei, Z.; Wang, Q.-M. Luminescent Molecular Ag−S Nanocluster $[Ag_{62}S_{13}(SBut)_{32}](BF_4)_4$. *J. Am. Chem. Soc.* **2010**, *132*, 17678−17679.

(36) Goswami, N.; Giri, A.; Bootharaju, M. S.; Xavier, P. L.; Pradeep, T.; Pal, S. K. Copper quantum clusters in protein matrix: potential sensor of Pb^{2+} ion. *Anal. Chem.* **2011**, *83*, 9676−9680.

(37) Wei, W.; Lu, Y.; Chen, W.; Chen, S. One-pot synthesis, photoluminescence, and electrocatalytic properties of subnanometer-sized copper clusters. *J. Am. Chem. Soc.* **2011**, *133*, 2060−2063.

(38) Yang, H.; Wang, Y.; Lei, J.; Shi, L.; Wu, X.; Mäkinen, V.; Lin, S.; Tang, Z.; He, J.; Häkkinen, H.; Zheng, L.; Zheng, N. Ligand-Stabilized $Au_{13}Cu_x$ (x= 2, 4, 8) Bimetallic Nanoclusters: Ligand Engineering to Control the Exposure of Metal Sites. *J. Am. Chem. Soc.* **2013**, *135*, 9568−9571.

(39) Yang, H.; Wang, Y.; Yan, J.; Chen, X.; Zhang, X.; Häkkinen, H.; Zheng, N. Structural Evolution of Atomically Precise Thiolated Bimetallic $[Au_{12+n}Cu_{32}(SR)_{30+n}]^{4-}$ (n= 0, 2, 4, 6) Nanoclusters. *J. Am. Chem. Soc.* **2014**, *136*, 7197−7200.

(40) Fields-Zinna, C. A.; Crowe, M. C.; Dass, A.; Weaver, J. E. F.; Murray, R. W. Mass spectrometry of small bimetal monolayer-protected clusters. *Langmuir* **2009**, *25*, 7704−7710.

(41) Negishi, Y.; Kurashige, W.; Niihori, Y.; Iwasa, T.; Nobusada, K. Isolation, structure, and stability of a dodecanethiolate-protected Pd_1Au_{24} cluster. *Phys. Chem. Chem. Phys.* **2010**, *12*, 6219−6225.

(42) Qian, H.; Jiang, D.-e.; Li, G.; Gayathri, C.; Das, A.; Gil, R. R.; Jin, R. Monoplatinum doping of gold nanoclusters and catalytic application. *J. Am. Chem. Soc.* **2012**, *134*, 16159−16162.

(43) Kwak, K.; Tang, Q.; Kim, M.; Jiang, D.-e.; Lee, D. Interconversion between Superatomic 6-electron and 8-electron Configurations of $M@Au_{24}(SR)_{18}$ Clusters (M= Pd, Pt). *J. Am. Chem. Soc.* **2015**, *137*, 10833−10840.

(44) Negishi, Y.; Iwai, T.; Ide, M. Continuous modulation of electronic structure of stable thiolate-protected Au_{25} cluster by Ag doping. *Chem. Commun.* **2010**, *46*, 4713−4715.

(45) Kurashige, W.; Munakata, K.; Nobusada, K.; Negishi, Y. Continuous modulation of electronic structure of stable thiolate-protected Au_{25} cluster by Ag doping. *Chem. Commun.* **2013**, *49*, 5447−5449.

(46) Negishi, Y.; Munakata, K.; Ohgake, W.; Nobusada, K. Effect of copper doping on electronic structure, geometric structure, and stability of thiolate-protected Au_{25} nanoclusters. *J. Phys. Chem. Lett.* **2012**, *3*, 2209−2214.

(47) Negishi, Y.; Igarashi, K.; Munakata, K.; Ohgake, W.; Nobusada, K. Palladium doping of magic gold cluster $Au_{38}(SC_2H_4Ph)_{24}$: formation of $Pd_2Au_{36}(SC_2H_4Ph)_{24}$ with higher stability than $Au_{38}(SC_2H_4Ph)_{24}$. *Chem. Commun.* **2012**, *48*, 660−662.

(48) Kumara, C.; Dass, A. AuAg alloy nanomolecules with 38 metal atoms. *Nanoscale* **2012**, *4*, 4084−4086.

(49) Kumara, C.; Dass, A. $(AuAg)_{144}(SR)_{60}$ alloy nanomolecules. *Nanoscale* **2011**, *3*, 3064−3067.

(50) Malola, S.; Hartmann, M. J.; Häkkinen, H. Copper Induces a Core Plasmon in Intermetallic $Au_{(144,145)-x}Cu_x(SR)_{60}$ Nanoclusters. *J. Phys. Chem. Lett.* **2015**, *6*, 515−520.

(51) Yan, J.; Su, H.; Yang, H.; Malola, S.; Lin, S.; Häkkinen, H.; Zheng, N. Total Structure and Electronic Structure Analysis of Doped Thiolated Silver $[MAg_{24}(SR)_{18}]^{2-}$ (M= Pd, Pt) Clusters. *J. Am. Chem. Soc.* **2015**, *137*, 11880−11883.

(52) Teo, B. K.; Zhang, H.; Shi, X. Site Preference in Vertex-Sharing Polyicosahedral Supraclusters Containing Groups 10 and 11 Metals and Their Bonding Implications: Syntheses and Structures of the First Au-Ag-M (M = Pt, Ni) Biicosahedral Clusters $[(Ph_3P)_{10}Au_{12}Ag_{12}PtCl_7]Cl$ and $[(Ph_3P)_{10}Au_{12}Ag_{12}NiCl_7](SbF_6)$. *Inorg. Chem.* **1994**, *33*, 4086−4097.

(53) Sharma, S.; Kurashige, W.; Nobusada, K.; Negishi, Y. Effect of trimetallization in thiolate-protected $Au_{24-n}Cu_nPd$ clusters. *Nanoscale* **2015**, *7*, 10606−10612.

(54) Yang, S.; Wang, S.; Jin, S.; Chen, S.; Sheng, H.; Zhu, M. A metal exchange method for thiolate-protected tri-metal $M1Ag_x Au_{24-x}(SR)$-$18°$ (M = Cd/Hg) nanoclusters. *Nanoscale* **2015**, *7*, 10005−10007.

(55) Wang, C.; Sasmaz, E.; Wen, C.; Lauterbach, J. Pd supported on $SnO_2-MnO_x-CeO_2$ catalysts for low temperature CO oxidation. *Catal. Today* **2015**, *258*, 481−486.

(56) Chen, H.; Ye, Z.; Cui, X.; Shi, J.; Yan, D. A novel mesostructured alumina−ceria−zirconia tri-component nanocomposite with high thermal stability and its three-way catalysis. *Microporous Mesoporous Mater.* **2011**, *143*, 368−374.

(57) Liu, H.; Zheng, Y.; Wang, G.; Qiao, S. A Three-Component Nanocomposite with Synergistic Reactivity for Oxygen Reduction Reaction in Alkaline Solution. *Adv. Energy Mater.* **2015**, *5*, 1401186.

(58) Zhang, J.; Li, K.; Zhang, B. Synthesis of dendritic Pt−Ni−P alloy nanoparticles with enhanced electrocatalytic properties. *Chem. Commun.* **2015**, *51*, 12012−12015.

(59) Sun, Y.; Mayers, B. T.; Xia, Y. Template-engaged replacement reaction: a one-step approach to the large-scale synthesis of metal nanostructures with hollow interiors. *Nano Lett.* **2002**, *2*, 481−485.

(60) Sun, Y.; Mayers, B. T.; Xia, Y. Metal nanostructures with hollow interiors. *Adv. Mater.* **2003**, *15*, 641−646.

(61) Zhang, L.; Wang, Y.; Tong, L.; Xia, Y. Synthesis of colloidal metal nanocrystals in droplet reactors: The pros and cons of interfacial adsorption. *Nano Lett.* **2014**, *14*, 4189−4194.

(62) Lu, X.; Tuan, H. Y.; Chen, J.; Li, Z. Y.; Korgel, B. A.; Xia, Y. Mechanistic studies on the galvanic replacement reaction between multiply twinned particles of Ag and HAuCl$_4$ in an organic medium. *J. Am. Chem. Soc.* **2007**, *129*, 1733−1742.

(63) Mandal, S.; Krishnan, K. M. Co core Au shell nanoparticles: evolution of magnetic properties in the displacement reaction. *J. Mater. Chem.* **2007**, *17*, 372−376.

(64) Wu, Z. Anti-Galvanic Reduction of Thiolate-Protected Gold and Silver Nanoparticles. *Angew. Chem., Int. Ed.* **2012**, *51*, 2934−2938.

(65) Yao, C.; Chen, J.; Li, M.-B.; Liu, L.; Yang, J.; Wu, Z. Adding two active silver atoms on Au$_{25}$ nanoparticle. *Nano Lett.* **2015**, *15*, 1281−1287.

(66) Liao, L.; Zhou, S.; Dai, Y.; Liu, L.; Yao, C.; Fu, C.; Yang, J.; Wu, Z. Mono-Mercury Doping of Au25 and the HOMO/LUMO Energies Evaluation Employing Differential Pulse Voltammetry. *J. Am. Chem. Soc.* **2015**, *137*, 9511−9514.

(67) Yao, C.; Lin, Y.; Yuan, J.; Liao, L.; Zhu, M.; Weng, L.; Yang, J.; Wu, Z. Mono-cadmium vs Mono-mercury Doping of Au25 Nanoclusters. *J. Am. Chem. Soc.* **2015**, *137*, 15350−15353.

(68) Tian, S.; Yao, C.; Liao, L.; Xia, N.; Wu, Z. Ion-precursor and ion-dose dependent anti-galvanic reduction. *Chem. Commun.* **2015**, *51*, 11773−11776.

(69) Wu, Z.; Suhan, J.; Jin, R. One-pot synthesis of atomically monodisperse, thiol-functionalized Au$_{25}$ nanoclusters. *J. Mater. Chem.* **2009**, *19*, 622−626.

(70) Li, M. B.; Tian, S. K.; Wu, Z.; Jin, R. Cu^{2+} induced formation of Au$_{44}$(SC$_2$H$_4$Ph)$_{32}$ and its high catalytic activity for the reduction of 4-nitrophenol at low temperature. *Chem. Commun.* **2015**, *51*, 4433−4436.

(71) Yao, C.; Tian, S.; Liao, L.; Liu, X.; Xia, N.; Yan, N.; Gan, Z.; Wu, Z. Synthesis of fluorescent phenylethanethiolated gold nanoclusters via pseudo-AGR method. *Nanoscale* **2015**, *7*, 16200−162003.

(72) Zhu, M.; Aikens, C. M.; Hollander, F. J.; Schatz, G. C.; Jin, R. Correlating the crystal structure of a thiol-protected Au25 cluster and optical properties. *J. Am. Chem. Soc.* **2008**, *130*, 5883−5885.

(73) Pei, Y.; Zeng, X. C. Investigating the structural evolution of thiolate protected gold clusters from first-principles. *Nanoscale* **2012**, *4*, 4054−4072.

(74) Tlahuice, A.; Garzon, I. L. On the structure of the Au$_{18}$(SR)$_{14}$ cluster. *Phys. Chem. Chem. Phys.* **2012**, *14*, 3737−3740.

(75) Yuan, Y.; Cheng, L.; Yang, J. Electronic Stability of Phosphine-Protected Au$_{20}$ Nanocluster: Superatomic Bonding. *J. Phys. Chem. C* **2013**, *117*, 13276−13282.

(76) Jiang, D.; Luo, W.; Tiago, M. L.; Dai, S. In search of a structural model for a thiolate-protected Au38 cluster. *J. Phys. Chem. C* **2008**, *112*, 13905−13910.

(77) Malola, S.; Lehtovaara, L.; Knoppe, S.; Hu, K.; Palmer, R. E.; Bürgi, T.; Häkkinen, H. Au$_{40}$(SR)$_{24}$ Cluster as a Chiral Dimer of 8-Electron Superatoms: Structure and Optical Properties. *J. Am. Chem. Soc.* **2012**, *134*, 19560−19563.

(78) Pei, Y.; Shao, N.; Gao, Y.; Zeng, X. C. Investigating Active Site of Gold Nanoparticle Au$_{55}$(PPh3)$_{12}$Cl$_6$ in Selective Oxidation. *ACS Nano* **2010**, *4*, 2009−2020.

(79) Kumara, C.; Aikens, C. M.; Dass, A. X-ray Crystal Structure and Theoretical Analysis of Au$_{25−x}$Ag$_x$(SCH$_2$CH$_2$Ph)$_{18}$−Alloy. *J. Phys. Chem. Lett.* **2014**, *5*, 461−466.

(80) Kauffman, D. R.; Alfonso, D.; Matranga, C.; Qian, H.; Jin, R. A Quantum Alloy: The Ligand-Protected Au$_{25−x}$Ag$_x$(SR)$_{18}$ Cluster. *J. Phys. Chem. C* **2013**, *117*, 7914−7923.

(81) Gottlieb, E.; Qian, H.; Jin, R. Atomic-Level Alloying and De-alloying in Doped Gold Nanoparticles. *Chem. - Eur. J.* **2013**, *19*, 4238−4243.

(82) Walter, M.; Akola, J.; Lopez-Acevedo, O.; Jadzinsky, P. D.; Calero, G.; Ackerson, C. J.; Whetten, R. L.; Gronbeck, H.; Hakkinen, H. A unified view of ligand-protected gold clusters as superatom complexes. *Proc. Natl. Acad. Sci. U. S. A.* **2008**, *105*, 9157−9162.

(83) Wu, Z.; Jin, R. The Observation of Gaseous Gold Superions Induced from Monodispersed Nanoparticles. *Chem. - Eur. J.* **2011**, *17*, 13966−13970.

(84) Lee, D.; Donkers, R. L.; Wang, G. L.; Harper, A. S.; Murray, R. W. Electrochemistry and optical absorbance and luminescence of molecule-like Au$_{38}$ nanoparticles. *J. Am. Chem. Soc.* **2004**, *126*, 6193−6199.

(85) Moskovits, M.; Di Lella, D. P. Surface-enhanced Raman spectroscopy of benzene and benzene-d$_6$ adsorbed on silver. *J. Chem. Phys.* **1980**, *73*, 6068−6075.

(86) Chen, L.; Gao, Y.; Cheng, Y.; Su, Y.; Wang, Z.; Li, Z.; Zhang, R.-Q. Strong Core@Shell Dependence in Surface-Enhanced Raman Scattering of Pyridine on Stable 13-Atom Silver-Caged Bimetallic Clusters. *J. Phys. Chem. C* **2015**, *119*, 17429−17437.

(87) Li, X.; Kiran, B.; Li, J.; Zhai, H. J.; Wang, L. S. Experimental Observation and Confirmation of Icosahedral W@Au12 and Mo@Au12 Molecules. *Angew. Chem., Int. Ed.* **2002**, *41*, 4786−4789.